Chip

A versatile optoelectronic device for ultrasensitive negative-positive pressure sensing applications

Xiaoshuai An[1,2], Sizhe Gui[1], Yingxin Li[1], Zhiqin Chu[2,3,*] & Kwai Hei Li[1,*]

[1]School of Microelectronics, Southern University of Science and Technology, Shenzhen 518055, China [2]Department of Electrical and Electronic Engineering, The University of Hong Kong, Pokfulam Road, Hong Kong 999077, China [3]School of Biomedical Sciences, The University of Hong Kong, Pokfulam Road, Hong Kong 999077, China

*E-mails: zqchu@eee.hku.hk (Zhiqin Chu), khli@sustech.edu.cn (Kwai Hei Li)

A versatile optoelectronic device with ultrasensitive negative-positive pressure sensing capabilities, which is integrated with a wireless monitoring system, was fabricated and demonstrated in the current work. The device comprises a monolithic GaN chip with a polydimethylsiloxane cavity and nanograting, which effectively transduces pressure stimuli into optical changes detected by the GaN chip. The developed device exhibits an ultra-low detection limit for a mass of 0.03 mg, a pressure of 2.94 Pa, and a water depth of 0.3 mm, with a detection range of −100 kPa to 30.5 kPa and high stability. The versatility of the device is demonstrated by its ability to monitor heart pulse, grip strength, and respiration. Its integration with a wireless data transmission system enables real-time monitoring of human activity and heart rate underwater, making it suitable for precise measurements in various practical applications.

INTRODUCTION

Pressure sensors have drawn considerable attention due to their wide range of applications, including healthcare monitoring[1-3], medical diagnosis[4], human-machine interfaces[5], and underwater motion tracking[6,7]. Various pressure-sensing mechanisms have been utilized, such as piezoresistive[8-10], capacitive[11-14], piezoelectric[15-17], and triboelectric[18,19]. Advanced techniques, including micro-/nano-engineering device structures and manipulating substrate materials, especially the emerging metal-organic framework (MOF) and MXene
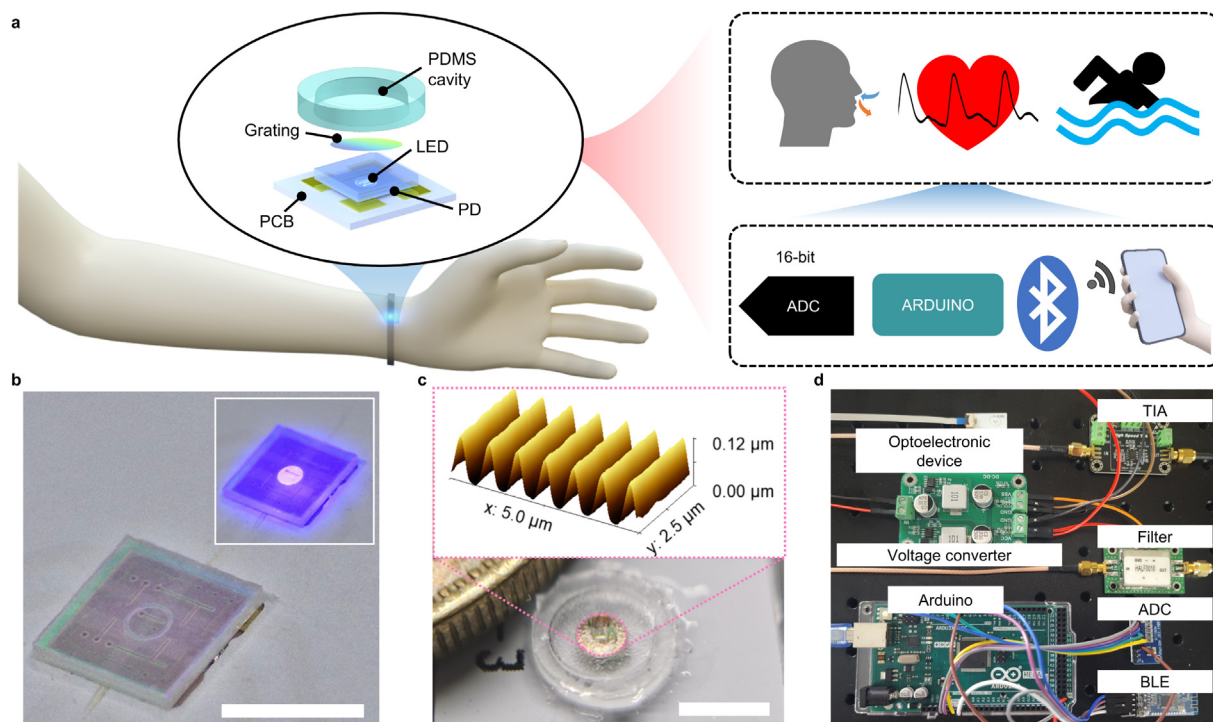
materials[20-24], have been utilized to enhance sensing capabilities. Notably, the optical pressure sensing mechanism, based on the principles of light-intensity induction and wavelength shift[25,26], has emerged as a promising alternative due to its rapid response, high sensitivity, and immunity to magnetic interference. The incorporation of advanced optical materials, such as YPO_4:Yb^{3+}−Er^{3+} and Ce^{3+}-doped fluorapatite-$Y_6Ba_4(SiO_4)_6F_2$ that can produce variable energy bands under applied pressures, have been proposed to enhance the sensing range and signal intensity[27,28]. However, current demonstrations of optical sensing systems encounter limitations due to their reliance on external light sources and complex operational procedures, which increases the cost and size of the system. Moreover, despite the growing importance of underwater motion tracking, the development of pressure sensing which is capable of effective functioning underwater still remains challenging. Electrically conductive materials suffer from corrosion and degradation when being in long-term contact with water, and incorporating a waterproofing package may lead to diminished sensitivity[6,29].

To overcome the existing limitations, an on-chip integration scheme is introduced, integrating the optical source and detector on a chip-scale platform[30-32]. GaN-based semiconductors are promising due to their long lifespan, swift response, and high efficiency[33,34]. This strategy has been employed in chip-scale devices for visible light communication and sensing applications[35,36]. However, a key challenge arises from the structural rigidity of typical optical GaN devices, which hinders their ability to detect ambient pressure fluctuations, particularly when monitoring human activities across both negative and positive pressure ranges.

This work presents a miniaturized pressure-sensing unit with a wireless monitoring system, as schematically illustrated in Fig. 1a. The device comprises a GaN chip with an light-emitting diode (LED) and photodetector (PD) fabricated through wafer-scale microfabrication techniques. A flexible polydimethylsiloxane (PDMS) cavity and nanogratings, which serve as the optical reflector, were incorporated into the design. Upon pressure stimuli, the deformation of the PDMS cavity and the subsequent modulation of light by the nano-gratings lead to a pronounced change in the light intensity coupled into the GaN chip. Additionally, the capability of the device to monitor human activities with real-time data wirelessly transmitted to the mobile end, is also demonstrated.

DESIGN OF THE OPTOELECTRONIC DEVICE

Fig. 1b illustrates the GaN chip packaged on a printed circuit board (PCB), while Fig. 1c depicts its assembly with the PDMS cavity.

Fig. 1 | Concept and structure of the proposed optoelectronic device and wireless system. **a**, Schematic diagram of the proposed optoelectronic device with a wireless monitoring system. **b**, Optical image of the GaN chip. The scale bar is 1 mm. Inset shows the GaN chip under operation. **c**, Optical image of the optoelectronic device. The scale bar is 3 mm. Inset is the AFM image showing the surface morphology of the DVD grating. **d**, Optical image showing the components of the wireless monitoring system. Abbreviation: AFM, atomic force microscopy.

The working mechanisms of the device are schematically depicted in Fig. 2a. The monolithic GaN chip is responsible for both light emission and light detection. As the inset in Fig. 2b and the emission spectrum in Fig. 2c, the wavelength and full width at half maximum of LEDs are measured as 437.9 nm and 16.6 nm. The photo-to-dark current ratio of the zero-biased PD when LED driven at 10 mA is calculated as 3.03×10^6, proving that the PD can effectively respond to the light intensity fluctuations from the LED. When the device suffers from positive ambient pressure, the PDMS film and the reflector shift downwards, thereby increasing the amount of PD-captured light. Conversely, negative pressure induces an upward movement of the film, diminishing the PD-captured light, and more light will escape outside. Therefore, the device operates by transducing pressure into alterations in light intensity, generating a photocurrent signal from the GaN chip.

The sensing performance of the device is highly dependent on the optical characteristics and positioning of the reflector. To investigate this, the photocurrent responses of the GaN chip with Al foil, recordable disc (CD) gratings, and digital versatile disc (DVD) gratings at varying distances were recorded, as shown in Fig. 2b. Given the inherent transparency of bare PDMS, a mild decrease in photocurrent of 6.9 µA is observed when positioned up to 3 mm away from the chip. The application of Al foil, CD gratings, and DVD gratings resulted in a notable increase in photocurrent variation, reaching 146.7 µA, 157.8 µA, and 196.6 µA, respectively.

The underlying causes of the discrepancies in photocurrent variations induced by different reflective films are investigated. As shown in Fig. 2c, the reflection spectra of light incident on CD and DVD gratings reveal a low reflectivity of 10% to 20% within the 410 to 445 nm wavelength range. This reduced reflectivity at normal incidence suggests the presence of a diffraction effect arising from the periodic structure of the films. To investigate this phenomenon, theoretical simulations were carried out to determine the effect of the nano-grating on the diffracted light intensity at various angles. The simulation models were constructed based on the nano-grating parameters measured by the atomic force microscopy (AFM), specifically line spacing and valley-to-peak height: 1490 nm and 143 nm for CD, and 740 nm, and 115 nm for DVD, respectively. The results in Fig. 2f indicate that besides the 0th order at 0°, intense light in the ±first orders for DVD and ±first and ±second orders for CD is distributed at larger angles due to the diffraction effect explaining the observed low reflectivity in the normal direction. Notably, unlike plane gratings, the largest diffracted efficiency shifts from the 0th to the ±first orders, resulting from the inclined blazed facet, which is highly influenced by the valley-to-peak values. A visual illustration of the diffracted angle from the grating is provided in Fig. S2.

Referring to calculating results and research report of the literature[37], ray-trace simulations for comparing different reflective films induced light intensity change in PD are conducted. The results show high consistency with the experimental result in Fig. 2b that DVD film leads to the largest signal intensity compared to the other reflective films, further proving that DVD grating is the preferred choice for constructing the versatile optoelectronic device (see Fig. S3).
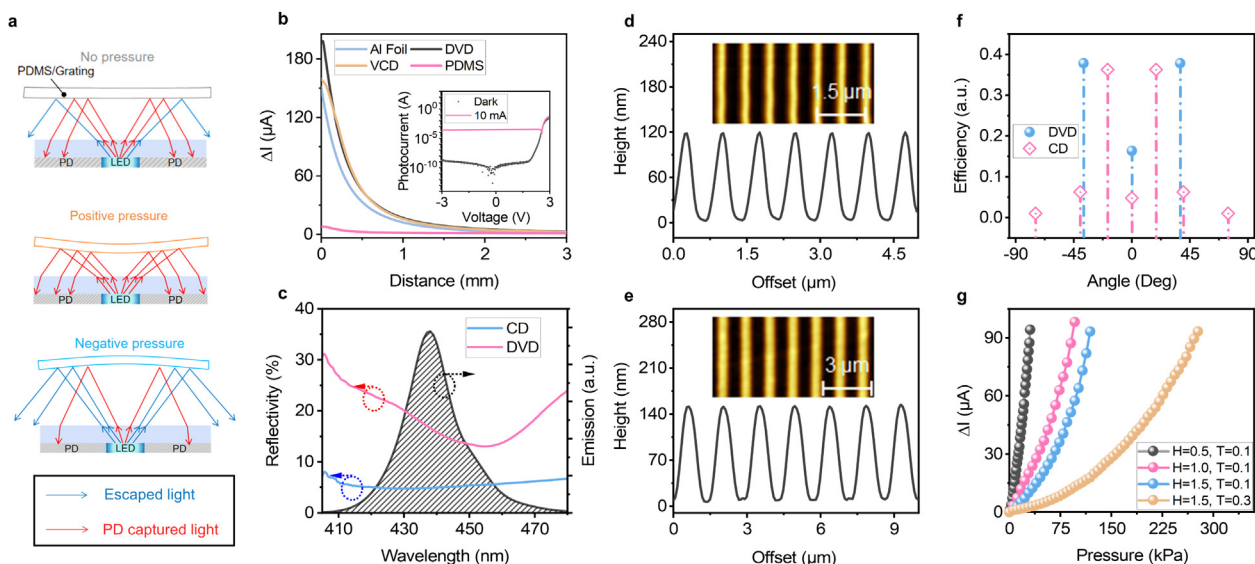
After determining DVD grating as the optical reflector, another crucial factor to consider is the structural parameters of the PDMS cavity, specifically the thickness (T) and the initial height (H), which govern the dynamic position of the reflector under varying pressure conditions. Given that the results presented in Fig. 2b indicate that films positioned at d < 1.5 mm can introduce a significant photocurrent change, four PDMS films with different combinations of T and H, ranging from millimeter to submillimeter scale (see Fig. S4), are equipped with the GaN chip for comparative analysis. The PDMS films are glued with a DVD grating with the same diameter of 1.5 mm.

The results presented in Fig. 2g via the setup in Fig. 3a indicate that the device configured with $T = 0.1$ mm and $H = 0.5$ mm exhibits a positive sensing range of 0 to 30.5 kPa, which is accompanied by a ΔI of 94.3 µA (where $\Delta I = I - I_0$, and I_0 is defined as the photocurrent before applying stimuli), demonstrating relatively high sensitivity. Additionally, the sensing range can be expanded by increasing T and H. For instance, as illustrated by the ΔI-pressure line in Fig. 2g, increasing H from 0.5 to 1.0 mm and subsequently to 1.5 mm results in the extension of the detection range to 96.2 and 118.8 kPa, respectively. This broadening is attributed to the increased deformation space provided by the enlarged H dimension at higher pressures. Similarly, thicker structures, which are achieved by increasing the other parameter T, can enhance the resistance to deformation and consequently increase the upper detection limit. It is noteworthy that there exists a trade-off between sensitivity and measurement range. Therefore, aiming to achieve high sensitivity in this work, the device with H and T of 0.1 mm and 0.5 mm, respectively, was selected for a systematic investigation of its sensing performance and potential applications.

SENSING PERFORMANCE OF THE OPTOELECTRONIC DEVICE

The pressure-sensing performance of the device is assessed by analyzing its photocurrent responses to positive pressure. In Fig. 3b, by applying linear regression to the measured data, the sensitivities are determined to be 1.95 and 3.56 µA/kPa within the pressure ranges of 0 to 10.2 kPa and 10.2 to 30.5 kPa, respectively, with R^2 values exceeding 0.98. Subsequently, the device is subjected to stepwise pressure changes. Fig. 3c illustrates the variation of ΔI as pressure increases from 5.9 to 23.4 kPa. Three cycles are plotted for all the pressure levels, demonstrating that the photocurrent value can return to its initial value and remain stable across all cycles. Moreover, the ΔI remains consistent among the three cycles for each applied pressure. As shown in Fig. 3d, stepwise increasing and decreasing pressures ranging from 0 to 23.1 kPa are applied to the device with a pressure-maintaining time of 6 s. The symmetry observed in the loading and unloading processes further indicates the stability of the device.

In addition to positive pressure sensing, the photocurrent response in the negative range of −100 to 0 kPa was examined via the setup in Fig. 3e and illustrated in Fig. 3f. As the PDMS/grating film moves away from the GaN chip during pumping, a reduced sensitivity is observed, which is consistent with the findings presented in Fig. 2b. To investigate the repeatability of the device, an instantaneous pumping and venting process was applied to realize a rapid pressure change, and response ΔI under negative pressures from −5 to −20 kPa are measured. As illustrated in Fig. 3g, the device rapidly responds to varying pressures and maintains consistency across three cycles. In Fig. 3h, a stepwise pumping and venting process was employed to produce the negative pressure of −1 to −30 kPa over a holding time of 20 s. The flat profile of

Fig. 2 | Design and optimization of the optoelectronic device. a, Schematic diagram of the working mechanism of the optoelectronic device for sensing pressures. **b,** Measured photocurrent of the GaN chip when moving the films placed at varying distances between 0 mm and 3 mm from the chip. The inset shows the response of PD to the light intensity from LED. **c,** Reflectance spectra of the CD and DVD gratings under normal incident light and the emission spectrum of the LED operated at 10 mA. **d−e,** AFM measured profiles of the DVD and CD gratings. **f,** Simulated results of diffraction efficiency of CD and DVD gratings. **g,** Photocurrent response of the device when using the PDMS cavities with different combinations of H and T. The H and T parameters in **g** are in millimeters. Abbreviations: PD, photodetector; LED, light-emitting diode; AFM, atomic force microscopy; PDMS, polydimethylsiloxane.

ΔI during the holding time and the symmetrical profile between the pumping and venting processes further demonstrate the stability and repeatability of the device. In Fig. 3g and h, the negative base pressure was set to −1 kPa, which is the minimum executable pressure of the commercial programmer. The small peaks in the two figures arise from the pressure fluctuations during the pressure adjustment, demonstrating the ability to monitor in real time. According to the results in Fig. 3d−h, the hysteresis is calculated to be as low as 1.12%, as shown in the Fig. S5.
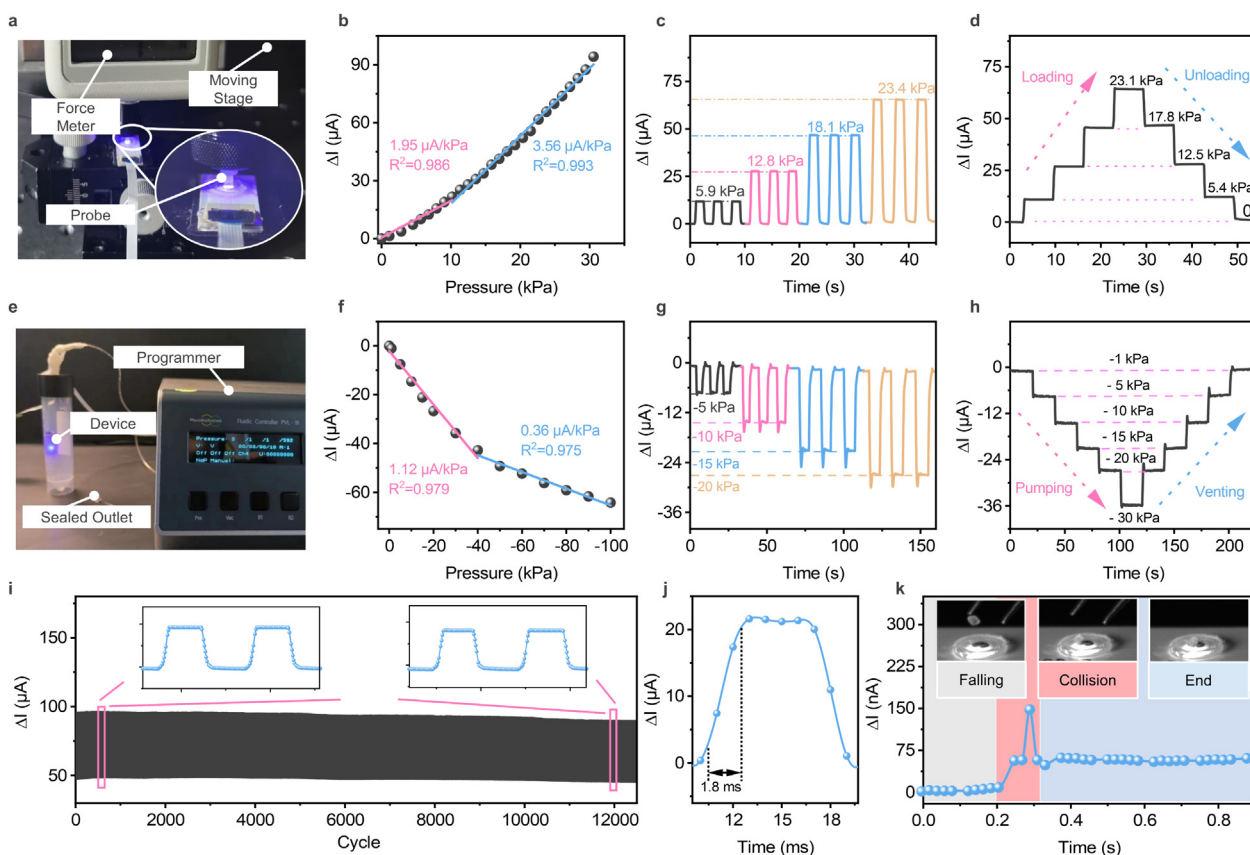
To further evaluate the device performance, a number of key parameters have been subjected to detailed analysis, including durability, response time and detection limit. For durability assessment, the device is subjected to over 12,000 cycles within a pressure range of 16.9 to 30.1 kPa. As shown in Fig. 3i, the response value remains consistent throughout the entire durability test, and the waveform shapes remain unaltered between the initial and final stages. Additionally, the transient response was investigated by mounting the device on the opposite side of a vibrating stage, which is loaded with a pulse signal of 100 Hz. As illustrated in Fig. 3j, the times to reach 10% to 90% and 90% to 10% of the maximum values were measured as 1.8 ms.

To assess the detection limit, a 0.3 mg sugar particle was released from a height of about 3 mm and fell onto the surface of the device. The falling process was captured by a high-speed camera as the inset of Fig. 3k. As illustrated in Fig. 3k, the response curve indicates a photocurrent change of 48.2 nA induced by the sugar mass, with a sharp peak of 148.3 nA detected due to collision momentum. Notably, the photocurrent change of 48.2 nA is significantly larger than the readable signals of 5 nA, suggesting a detection limit as low as 0.03 mg (equivalent to ~300 nN).

APPLICATIONS IN DIVERSE SCENARIOS

The underwater pressure-sensing ability of the device is evaluated by affixing it to the base of a cylindrical glass tank and gradually introducing water. Photocurrent alterations are recorded at 10-cm intervals. As shown in Fig. 4a, a total ΔI of 24.1 μA is obtained across a water level change from 0 cm to 100 cm, corresponding to a positive pressure of 9.8 kPa. Based on these results, which indicate a ΔI of 94.3 μA at 30.5 kPa, the maximum detecting water depth is estimated to be approximately 3 m. Additionally, Fig. 4b demonstrates the consistent photocurrent responses across cycles when changing depth periodically by 1 mm, 3 mm, and 5 mm, highlighting high repeatability in tracking vertical underwater movements. To investigate its sensing resolution, the device is mounted on a motorized stage and immersed in water at an initial depth of 3.5 cm. Clear response profiles are observed when manipulating the device movement in a pulsed and stepwise manner within a range of 0.3 mm,

Fig. 3 | **Characterizations when loading and unloading pressures on the sensor. a,** Experimental setup for testing the response of the device to positive pressures. **b,** Photocurrent changes as a function of positive pressure. Dynamic photocurrent responses when loading **c,** instantaneous and **d,** stepwise positive pressure changes. **e−h,** Photocurrent responses when applying negative pressure for testing the dynamic performance corresponding to **a-d**. **i,** Cyclic measurement when pressure changes from 16.9 to 30.1 kPa. **j,** Transient response of the device. **k,** Photocurrent changes when dropping a 0.3-mg sugar particle on the device. The inset shows optical images captured during the particle fall.

corresponding to a pressure change of 2.94 Pa and a ΔI of 4.8 nA, as presented in Fig. 4c. Thanks to its high sensing resolution, the device also responds to subtle pressure changes arising from the water surface. As illustrated in the photocurrent curve in Fig. 4d, a distinct oscillation process can be detected when gently blowing the water surface.

The versatility of the device in practical applications was explored by taking advantage of its compact structure, miniaturized dimensions, and highly sensitive performance. The monitoring of heart pulse is a particular focus due to its potential for reflecting health information and preventing cardiovascular diseases. Four representative arterial pulse signals were selected for testing, including those from the ankle artery region (DAF), the radial artery (RA), the brachial artery (BA), and the temporal artery (TA). As shown in Fig. 4e, discernible waveform profiles are observed, which facilitates the extraction of pertinent information regarding blood pressure, heart rate, volume, and rhythm through subsequent analysis[38]. To verify its capability to operate under low-power consumption, an examination was conducted in which the device was operated at a very low current of 10 µA. The comparison shown in Fig. 4f illustrates the clear distinction of three peaks (the percussion wave (P), the late systolic pulse waveform (T), and the diastolic pulse waveform (D)) and two phases (systole and diastole), demonstrating the capability of the device to operate with an ultra-low power consumption of 25.2 µW. Additionally, obvious heart pulse signals can be observed during motion due to the 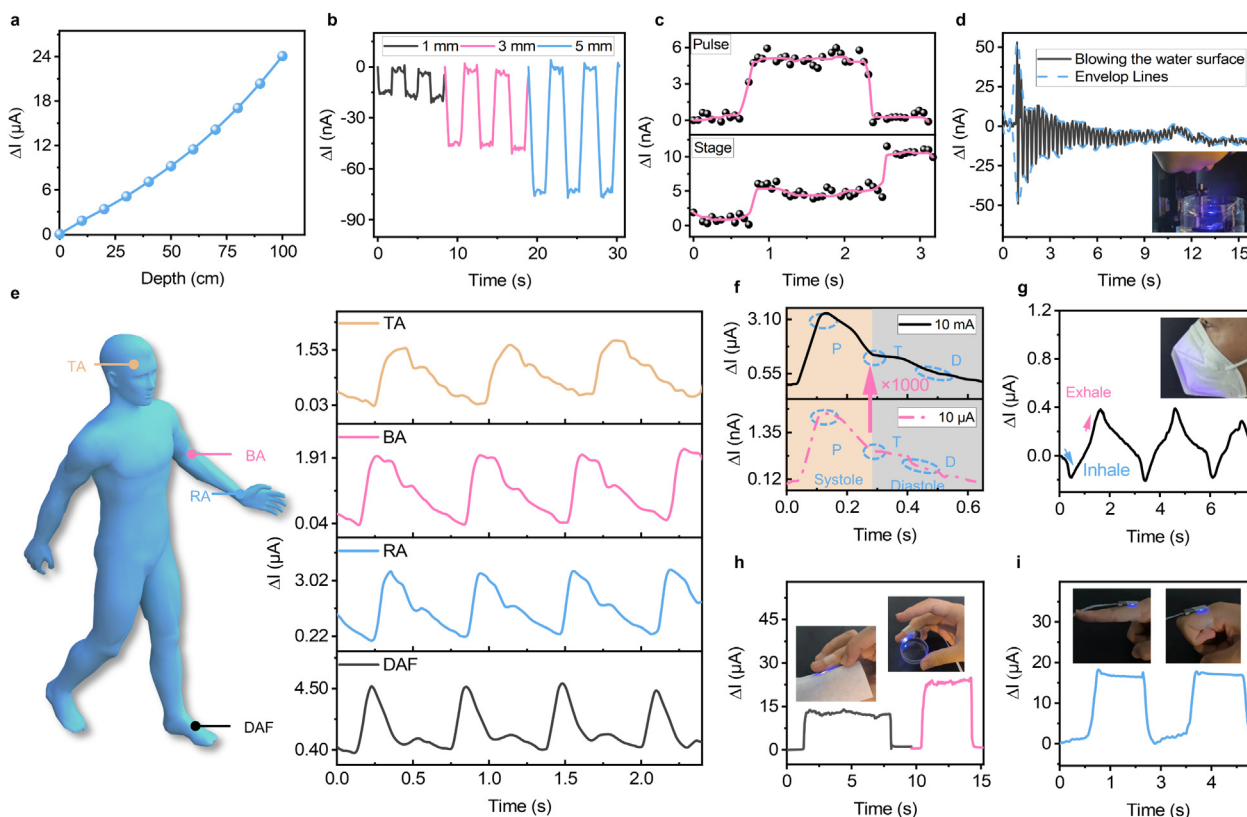tight contact of the device to the skin, which suggests that the device suffers a relatively slight influence from motion artifacts (see Fig. S6).

Additionally, the sensitivity of the device to subtle pressure variations induced by human respiration was exhibited when placing the device inside a mask, as depicted in Fig. 4g. This highlights its capability to distinguish between inhalation and exhalation phases by monitoring pressure alterations during the respiratory cycle. Moreover, its abilities for gripping force and finger bending detection were validated by mounting it on the different positions of fingers, with the photocurrent responses plotted in Fig. 4h and i.

A comparative overview of Table 1 indicates that the proposed device demonstrates advantageous characteristics of compact size, a wide sensing range of −100 to 30.5 kPa, a short response time of 1.8 ms, and the capability to operate in both air and underwater environments.

WIRELESSLY MONITORING HUMAN ACTIVITIES UNDERWATER

In contrast to wired operation, the implementation of wireless operation for the device enhances the convenience and expands the scope of operational scenarios, particularly in monitoring human activity underwater. To achieve this objective, a wireless monitoring system was constructed,

Fig. 4 | Performance of the optoelectronic when monitoring human activity and physiological signals. a, Photocurrent response for monitoring water level ranging from 0 to 100 cm. **b,** Photocurrent response when periodically moving the device in depths of 1 mm, 3 mm, and 5 mm. **c,** Characterizations for measuring resolution of water level when operating underwater. **d,** Measured photocurrent response curve when blowing the water surface. **e,** Schematic diagram and photocurrent waveforms collected from different artery positions by the device. **f,** Comparison when LED biased at 10 mA and 10 µA. **g–i,** Photocurrent changes when applying a device to detect the pressure changes induced by breathing in the mask, gripping force of holding a paper and a Petri dish, and muscular pressure induced by bending fingers. Abbreviation: LED, light-emitting diode.

Table 1 | Comparison with previously reported pressure sensors

Sensing principle	Detection limits	Resolution	Sensing range	N/P pressure	Response time	Size	Underwater
Piezoresistive[39]	20 mg	NR	0−10 kPa	P	NR	1 × 1 cm^2	No
Piezoresistive Capacitive[40]	65 mg	NR	S: 0−0.15 N P: 0−25 N	P	100 ms	1 × 1 cm^2	No
Piezoresistive[41]	NR	NR	0−400 Pa	P	NR	1 × 2 cm^2	No
Capacitive[42]	17.8 mg/1.78 Pa	NR	1.7−1000 kPa	P	30−60 ms	cm scale	No
Optical[43]	NR	~50 Pa	100 kPa	NR	NR	NR	No
Optical fiber[44]	30 Pa	NR	NR	P	<20 ms	cm scale	No
Optical fiber[45]	NR	NR	NR	P	NR	7.62 × 2.54 cm	No
Optical fiber[46]	1 mg/7 mPa	NR	0−2 Pa	P	20 µs	cm scale	No
Piezoresistive[6]	98 Pa	1 cm	1−40 cm	P	289 ms	cm scale	Yes
Optical fiber[47]	NR	0.06 N	1−50 cm	P	NR	Φ 30−50 mm	Yes
Capacitive[14]	100 Pa	NR	−98−100 kPa	N−P	250/420 ms	cm scale	Air
Capacitive[12]	NR	NR	−60 − 20 kPa	N−P	NR	cm scale	Air
Optoelectronic (This work)	0.03 mg	2.94Pa /0.3 mm	−100 − 30.5 kPa/0.3−300 cm	N−P	1.8 ms	Φ4 mm	Yes

which incorporates Arduino and bluetooth low energy (BLE) devices, with the schematic illustrated in Fig. 5a. To ensure adequate data precision in accordance with the nanoampere scale resolution capabilities of the device, a 16-bit analog-to-digital converter (ADC) was employed and connected to the general-purpose input/output port via the inter-integrated circuit communication protocol. Additionally, the level of undesirable noise from the Arduino system was significantly mitigated through the combined application of a filtering algorithm and a low-pass filtering circuit. To facilitate real-time data acquisition and visualization, a mobile application was developed for smartphone interfaces.

Fig. 5b and S2 illustrate the real-time monitoring capability of the integrated system for underwater human activities, demonstrating three distinct modes of movement. Motion tracks for slow and quick sinking and rising within the ranges of 0 to 400 mm and 0 to 50 mm, respectively, are presented, with an apparent monitoring curve observable on the smartphone. Stepwise processes with precise intervals are also shown, which highlights the ability of the device to determine depth and maintain temporal tracking. Additionally, Fig. 5c and S3 in Appendix A present the measurement of heart pulse collected from a volunteer. By collecting approximately 40 points per second, the waveforms reveal sufficient
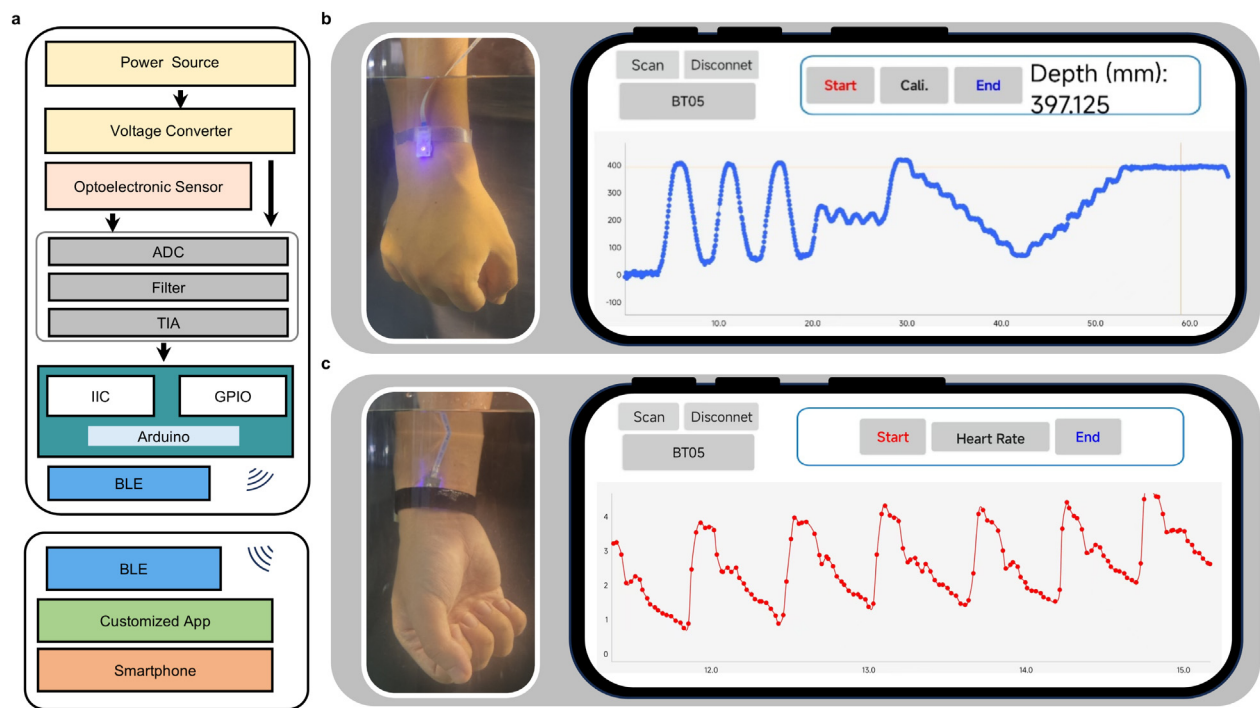

Fig. 5 | Wirelessly monitoring the human movement and heart pulse underwater. a, Schematic diagram showing the design of the wireless monitoring system. **b−c,** Photograph and received data when real-time monitoring human movement and heart pulse underwater.

physiological information, including peak intensities, systolic and diastolic durations, and heart rate. Detailed demonstration videos are available in the Supplementary material.

CONCLUSION

In summary, an optoelectronic device integrated with a wireless monitoring system was presented in the current work. The device incorporates a monolithic GaN chip, a PDMS cavity, and a nanograting film to form a pressure-sensing unit. Through optimization, the device exhibits a wide measurement range from −100 to 30.5 kPa and a low detection limit of 0.03 mg. Moreover, the device has been tested in an underwater environment, demonstrating its ability to detect minute variations in water levels as small as 0.3 mm, which is equivalent to a subtle pressure of 2.94 Pa. Its versatility was evidenced by the real-time monitoring of heart pulse, gripping force, and breath. This work presents a novel design perspective for developing high-performance pressure-sensing units based on GaN optoelectronics, with the potential for diverse practical applications.

METHODS

Fabrication of the GaN chip   The wafer, consisting of 2-μm-thick undoped GaN, 3-μm-thick Si-doped n-GaN, eight pairs of 2.5-nm-thick InGaN/10-nm-thick GaN multiple quantum wells, 50-nm-thick AlGaN, and 50-nm-thick Mg-doped p-GaN, was grown by metal-organic chemical vapor deposition on a 4-inch sapphire substrate. After forming the mesa regions of LED and PD through photolithography and Cl_2-based inductively coupled plasma (ICP), a 120-nm-thick indium-tin-oxide (ITO) was deposited on p-GaN. Another ICP process was followed to remove the GaN areas between the LED and PD. The p- and n-electrodes were then coated on the GaN wafer by electron-beam evaporation. SiO_2 layers used to passivate the sidewall were deposited via plasma-enhanced chemical vapor deposition (PECVD) and distributed Bragg reflector (DBR) consisting of 23 pairs Ti_3O_5/SiO_2 were coated by an optical thin film coater, respectively. To expose the electrodes, SiO_2/DBRs were selectively etched by ICP. The combination of photolithography and e-beam deposition was employed to form the n- and p-pads. Detailed fabrication flow can be found in Fig. S1a. After the sapphire was polished to 150 μm, the wafer was diced into 1×1 mm^2 pieces and flip-chip bonded to PCB.

Preparation of the metal reflecting gratings   The process of the reflecting gratings involves fragmenting an optical disc (Verbatim DVD-R) and then removing its cover to expose the metal layer. The metal layer was then peeled off and rinsed with acetone to remove the adhesive on its surface. To facilitate the handling of the thin-film grating, a layer of PDMS was poured onto the metal grating and cured at the temperature of 80 °C for 20 min. The metal-reflection-grating-on-PDMS was then placed under a laser to precisely define the sample dimensions. Subsequently, the Φ1.5 mm reflection grating was readily removed by immersing it in acetone and ethanol.

Preparation of the polydimethylsiloxane cavities   Resin molds used for repeatable pattern transfer were created using a high-resolution 3D printer (Form 3+). PDMS gel, with a prepolymer to curing agent ratio of 10 : 1, was poured into the mold and then placed in a vacuum environment for 20 min. Afterwards, the sample was heated at 80 °C for 30 min and 120 °C for 10 min to completely cure the PDMS cavity. Finally, the PDMS cavity was peeled off from the mold. The PDMS cavities of varying combinations of height (H) and thickness (T) were prepared.

Assembly of the pressure sensing device   The nanograting film was adhered to the PDMS cavity using PDMS gel and subjected to a negative pressure environment for 2 h to ensure tight connections. After aligning the PDMS cavity with the GaN chip, the PDMS gel was then employed to glue them together and follow with a cure process at 80 °C for 30 min to form the robust connection. The detailed fabrication process can be found in Fig. S1b.

Characterizations and measurements   The LED was driven at a constant current of 10 mA with the adoption of a source meter (2450, Keithley), and the photocurrent of the unbiased PD was measured using a multimeter (DMM6500, Keithley). The positive pressure was measured by a calibrated force meter (DS2-5N, MOTIVE) with a fixed contact region of Φ1.5 mm to the PDMS surface. The negative pressure was generated by a vacuum pump, monitored, and adjusted by a programmable controller (PVLIII) and a vacuum kettle with a valve. The morphologies of the gratings were characterized by AFM (NanoWizard 4XP, Bruker). The reflectance spectra of the film and the emission spectra of the LED were measured using a spectrometer (Mayapro 2000, Ocean Optics) and a lux meter (OHSP350B), respectively.

REFERENCES

1. Li, Y., Samad, Y. A. & Liao, K. From cotton to wearable pressure sensor. *J. Mater. Chem. A* **3**, 2181−2187 (2015). https://doi.org/10.1039/c4ta05810k.

2. Zang, Y., Zhang, F., Di, C.-a. & Zhu, D. Advances of flexible pressure sensors toward artificial intelligence and health care applications. *Mater. Horiz.* **2**, 140−156 (2015). https://doi.org/10.1039/C4MH00147H.

3. Mishra, S., Mohanty, S. & Ramadoss, A. Functionality of flexible pressure sensors in cardiovascular health monitoring: a review. *ACS Sens.* **7**, 2495−2520 (2022). https://doi.org/10.1021/acssensors.2c00942.

4. Farooq, M. et al. Thin-film flexible wireless pressure sensor for continuous pressure monitoring in medical applications. *Sensors* **20**, 6653 (2020). https://doi.org/10.3390/s20226653.

5. Lu, L., Jiang, C., Hu, G., Liu, J. & Yang, B. Flexible noncontact sensing for human-machine interaction. *Adv. Mater.* **33**, 2100218 (2021). https://doi.org/10.1002/adma.202100218.

6. Ni, Y. et al. Robust superhydrophobic rGO/PPy/PDMS coatings on a polyurethane sponge for underwater pressure and temperature sensing. *ACS Appl. Mater. Interfaces* **13**, 53271−53281 (2021). https://doi.org/10.1021/acsami.1c17165.

7. Zhou, X. et al. Gel-based strain/pressure sensors for underwater sensing: sensing mechanisms, design strategies and applications. *Compos. B: Eng.* **255**, 110631 (2023). https://doi.org/10.1016/j.compositesb.2023.110631.

8. Shi, J. et al. Multiscale hierarchical design of a flexible piezoresistive pressure sensor with high sensitivity and wide linearity range. *Small* **14**, 1800819 (2018). https://doi.org/10.1002/smll.201800819.

9. Tran, A. V., Zhang, X. & Zhu, B. The development of a new piezoresistive pressure sensor for low pressures. *IEEE Trans. Ind. Electron.* **65**, 6487−6496 (2018). https://doi.org/10.1109/tie.2017.2784341.

10. Zhao, X.-H. et al. Skin-inspired highly sensitive tactile sensors with ultrahigh resolution over a broad sensing range. *ACS Appl. Mater. Interfaces* **15**, 30486−30494 (2023). https://doi.org/10.1021/acsami.3c04526.

11. Kwon, D. et al. Highly sensitive, flexible, and wearable pressure sensor based on a giant piezocapacitive effect of three-dimensional microporous elastomeric dielectric layer. *ACS Appl. Mater. Interfaces* **8**, 16922−16931 (2016). https://doi.org/10.1021/acsami.6b04225.

12. Shi, H. et al. Screen-printed soft capacitive sensors for spatial mapping of both positive and negative pressures. *Adv. Funct. Mater.* **29**, 1903020 (2019). https://doi.org/10.1002/adfm.201903020.

13. Ha, K.-H. et al. Highly sensitive capacitive pressure sensors over a wide pressure range enabled by the hybrid responses of a highly porous nanocomposite. *Adv. Mater.* **33**, 2103320 (2021). https://doi.org/10.1002/adma.202103320.

14. Zhang, M. et al. Flexible wearable capacitive sensors based on ionic gel with full-pressure ranges. *ACS Appl. Mater. Interfaces* **15**, 15884−15892 (2023). https://doi.org/10.1021/acsami.3c00916.

15. Wang, A., Hu, M., Zhou, L. & Qiang, X. Self-powered wearable pressure sensors with enhanced piezoelectric properties of aligned P(VDF-TrFE)/MWCNT composites for monitoring human physiological and muscle motion signs. *Nanomaterials* **8**, 1021 (2018). https://doi.org/10.3390/nano8121021.

16. Li, H., Liu, J., Li, K., Deng, J. & Liu, Y. Development of a high differential pressure piezoelectric active proportional regulation valve using a bending transducer. *IEEE Trans. Ind. Electron.* **68**, 12513−12523 (2020). https://doi.org/10.1109/TIE.2020.3044814.

17. Tan, Y. et al. High-performance textile piezoelectric pressure sensor with novel structural hierarchy based on ZnO nanorods array for wearable application. *Nano Res.* **14**, 3969−3976 (2021). https://doi.org/10.1007/s12274-021-3322-2.

18. Chen, G., Au, C. & Chen, J. Textile triboelectric nanogenerators for wearable pulse wave monitoring. *Trends Biotechnol.* **39**, 1078−1092 (2021). https://doi.org/10.1016/j.tibtech.2020.12.011.

19. Guo, W.-T. et al. Printed-scalable microstructure BaTiO₃/ecoflex nano-composite for high-performance triboelectric nanogenerators and self-powered human-machine interaction. *Nano Energy* **131**, 110324 (2024). https://doi.org/10.1016/j.nanoen.2024.110324.

20. Ha, M. et al. Bioinspired interlocked and hierarchical design of ZnO nanowire arrays for static and dynamic pressure-sensitive electronic skins. *Adv. Funct. Mater.* **25**, 2841−2849 (2015). https://doi.org/10.1002/adfm.201500453.

21. Li, X., Koh, K. H., Farhan, M. & Lai, K. W. C. An ultraflexible polyurethane yarn-based wearable strain sensor with a polydimethylsiloxane infiltrated multilayer sheath for smart textiles. *Nanoscale* **12**, 4110−4118 (2020). https://doi.org/10.1039/c9nr09306k.

22. Lai, Q.-T. et al. Emerging MXene-based flexible tactile sensors for health monitoring and haptic perception. *Small* **19**, 2300283 (2023). https://doi.org/10.1002/smll.202300283.

23. Sun, Q.-J. et al. Rise of metal-organic frameworks: from synthesis to E-skin and artificial intelligence. *ACS Appl. Mater. Interfaces* **16**, 45830−45860 (2024). https://doi.org/10.1021/acsami.4c07732.

24. Liu, S.-Z. et al. Recent progress on flexible self-powered tactile sensing platforms for health monitoring and robotics. *Small* **20**, 2405520 (2024). https://doi.org/10.1002/smll.202405520.

25. Vorathin, E., Hafizi, Z. M., Ismail, N. & Loman, M. Review of high sensitivity fibre-optic pressure sensors for low pressure sensing. *Opt. Laser Technol.* **121**, 105841 (2020). https://doi.org/10.1016/j.optlastec.2019.105841.

26. Sartiano, D. & Sales, S. Low cost plastic optical fiber pressure sensor embedded in mattress for vital signal monitoring. *Sensors* **17**, 2900 (2017). https://doi.org/10.3390/s17122900.

27. Runowski, M., Wozny, P. & Martín, I. R. Optical pressure sensing in vacuum and high-pressure ranges using lanthanide-based luminescent thermometer-manometer. *J. Mater. Chem. C* **9**, 4643−4651 (2021). https://doi.org/10.1039/d1tc00709b.

28. Runowski, M., Woźny, P., Stopikowska, N., Guo, Q. & Lis, S. Optical pressure sensor based on the emission and excitation band width (fwhm) and luminescence shift of Ce³⁺-doped fluorapatite-high-pressure sensing. *ACS Appl. Mater. Interfaces* **11**, 4131−4138 (2019). https://doi.org/10.1021/acsami.8b19500.

29. Li, L., Bai, Y., Li, L., Wang, S. & Zhang, T. A superhydrophobic smart coating for flexible and wearable sensing electronics. *Adv. Mater.* **29**, 1702517 (2017). https://doi.org/10.1002/adma.201702517.

30. Li, K. H. et al. Monolithically integrated InGaN/GaN light-emitting diodes, photodetectors, and waveguides on si substrate. *Optica* **5**, 564−569 (2018). https://doi.org/10.1364/Optica.5.000564.

31. Wang, Y. et al. Full-duplex light communication with a monolithic multicomponent system. *Light: Sci. Appl.* **7**, 83 (2018). https://doi.org/10.1038/s41377-018-0083-0.

32. Li, K. H., Lu, H., Fu, W. Y., Cheung, Y. F. & Choi, H. W. Intensity-stabilized LEDs with monolithically integrated photodetectors. *IEEE Trans. Ind. Electron.* **66**, 7426−7432 (2018). https://doi.org/10.1109/TIE.2018.2873522.

33. Wong, M. S., Nakamura, S. & DenBaars, S. P. Review—progress in high performance III-nitride micro-light-emitting diodes. *ECS J. Solid State Sci. Technol.* **9**, 015012 (2019). https://doi.org/10.1149/2.0302001jss.

34. Yuvaraja, S., Khandelwal, V., Tang, X. & Li, X. Wide bandgap semiconductor-based integrated circuits. *Chip* **2**, 100072 (2023). https://doi.org/10.1016/j.chip.2023.100072.

35. Hou, Y. et al. A versatile, incubator-compatible, monolithic GaN photonic chipscope for label-free monitoring of live cell activities. *Adv. Sci.* **9**, 2200910 (2022). https://doi.org/10.1002/advs.202200910.

36. Lee, Y.-J. et al. Monolithic integration of GaN-based light-emitting diodes and metal-oxide-semiconductor field-effect transistors: reply. *Opt. Express* **26**, A110−A110 (2018). https://doi.org/10.1364/OE.26.00A110.

37. Pozzobon, V., Levasseur, W., Do, K.-V., Palpant, B. & Perré, P. Household aluminum foil matte and bright side reflectivity measurements: application to a photobioreactor light concentrator design. *Biotechnol. Rep.* **25**, e00399 (2020). https://doi.org/10.1016/j.btre.2019.e00399.

38. Meng, K. Y. et al. Wearable pressure sensors for pulse wave monitoring. *Adv. Mater.* **34**, 2109357 (2022). https://doi.org/10.1002/adma.202109357.

39. Mu, C. et al. Flexible normal-tangential force sensor with opposite resistance responding for highly sensitive artificial skin. *Adv. Funct. Mater.* **28**, 1707503 (2018). https://doi.org/10.1002/adfm.201707503.

40. Zeng, X. et al. A bioinspired three-dimensional integrated e-skin for multiple mechanical stimuli recognition. *Nano Energy* **92**, 106777 (2022). https://doi.org/10.1016/j.nanoen.2021.106777.

41. Wang, D. et al. Freestanding silver/polypyrrole composite film for multifunctional sensor with biomimetic micropattern for physiological signals monitoring. *Chem. Eng. J.* **404**, 126940 (2021). https://doi.org/10.1016/j.cej.2020.126940.

42. Li, P. et al. Skin-inspired large area iontronic pressure sensor with ultra-broad range and high sensitivity. *Nano Energy* **101**, 107571 (2022). https://doi.org/10.1016/j.nanoen.2022.107571.

43. Dai, G. et al. Perovskite quantum dots based optical fabry-perot pressure sensor. *ACS Photonics* **7**, 2390−2394 (2020). https://doi.org/10.1021/acsphotonics.0c01109.

44. Li, J.-H., Chen, J.-H. & Xu, F. Sensitive and wearable optical microfiber sensor for human health monitoring. *Adv. Mater. Technol.* **3**, 1800296 (2018). https://doi.org/10.1002/admt.201800296.

45. Pan, J., Zhang, Z., Jiang, C., Zhang, L. & Tong, L. A multifunctional skin-like wearable optical sensor based on an optical micro-/nanofibre. *Nanoscale* **12**, 17538−17544 (2020). https://doi.org/10.1039/d0nr03446k.

46. Zhang, L. et al. Ultrasensitive skin-like wearable optical sensors based on glass micro/nanofibers. *Opto-Electron. Adv.* **3**, 190022 (2020). https://doi.org/10.29026/oea.2020.190022.

47. Leal-Junior, A. G. et al. Optimizing linearity and sensitivity of 3D-printed diaphragms with chirped FBGs in CYTOP fibers. *IEEE Access* **8**, 31983−31991 (2020). https://doi.org/10.1109/Access.2020.2973187.

MISCELLANEA

Author contributions   **Xiaoshuai An:** Writing – original draft, Methodology, Investigation, Data curation. **Sizhe Gui:** Methodology. **Yingxin Li:** Methodology. **Zhiqin Chu:** Writing – review & editing, Supervision, Resources, Funding acquisition. **Kwai Hei Li:** Writing – review & editing, Supervision, Resources, Funding acquisition, Conceptualization.